

# Simulations of a $2 \times 1.5D$ coded aperture camera for X-ray astronomy

J.J.M. in 't Zand<sup>1</sup>, L. Kuiper<sup>1</sup>, F. Ceraudo<sup>2</sup>, Y. Evangelista<sup>2</sup>, M. Hernanz<sup>3,4</sup>, and A. Patruno<sup>3</sup>

<sup>1</sup> SRON Space Research Organization Netherlands, Niels Bohrweg 4, 2333 CA Leiden, the Netherlands

<sup>2</sup> INAF-IAPS Roma, via Fosso del Cavaliere 100, 00133 Rome, Italy

<sup>3</sup> Institute of Space Sciences (ICE-CSIC), Campus UAB, 08193 Cerdanyola del Vallès (Barcelona), Spain

<sup>4</sup> Institut d'Estudis Espacials de Catalunya (IEEC), Barcelona, Spain

March 19, 2026

## ABSTRACT

The concept of two perpendicular one-dimensional coded aperture cameras, necessitated by the imaging capability of the detector, finds its application in the design of the Wide Field Monitor (WFM). This instrument has the future goal to monitor the variable X-ray sky for transient activity. Characteristic of each camera is a fine angular resolution in one direction (typically 5 arcmin) and a coarse one in the other (5 degrees). The coarse perpendicular resolution makes the camera so-called '1.5D'. The WFM has been studied for a number of space-borne X-ray observatory concepts: LOFT, eXTP, Strobe-X, ARCO and now LEM-X. We here report on a study of two decoding algorithms for this instrument and its imaging performance. Detector responses to the X-ray sky are simulated, including the signal processing by the front-end and back-end electronics. The decoding algorithms are the iterative removal of sources (IROS), in combination with cross correlation, and the maximum likelihood method (MLM). IROS is most suited for the determination of the point source configuration of the observed sky and MLM for the optimum determination of the source fluxes. The simulation results show that despite the 1.5D imaging of each camera, the reconstruction of scientific data is as if each camera pair were replaced by a single 2D camera with the same specification in angular resolution and a detector size equal to that of the two in the pair, except that source confusion is somewhat larger in the former. Thus, the WFM is a high performance monitoring instrument with straightforward and proven technology that enables the identification of new cosmic X-ray sources, for instance X-ray novae, gamma-ray bursts and electromagnetic counterparts to gravitational wave events from merging compact objects, and the detection of unusual and interesting behavior of persistent cosmic X-ray sources, such as accretion disk state changes.

**Key words.** Astronomical instrumentation: miscellaneous - Methods: numerical - Techniques: image processing - telescopes

## 1. Introduction

Apart from rotation, the sky seems static by the naked eye but is by far not. Particularly in X-rays, it is vibrant with variability and transient activity on all time scales. This became clear already early on in the 1960s at the dawn of X-ray astronomy, through instrumentation specifically designed for detecting transient activity on Earth (atmospheric nuclear weapons tests) through the Vela satellites (e.g., Klebesadel et al. 1973). This motivated the implementation of a long series of X-ray all-sky monitors (ASMs) throughout history, the most recent examples being the Monitoring All-sky X-ray Imager MAXI launched in 2009 to the International Space Station (ISS; Matsuoka et al. 2009), the cubesats Ninjasat (Tamagawa et al. 2025) and Blackcat (Falcone et al. 2024), the Wide Field X-ray Telescope (WXT) on the Einstein Probe (EP) launched in 2024 (Yuan et al. 2022) and ECLAIRs on the Space Variable Objects Monitor (SVOM; Godet et al. 2014; Givaudan et al. 2024) also launched in 2024. This will continue in the future. The modernization of the ASM fleet concentrates on the extension of the bandpass to longer wavelengths than the classical X-ray regime, i.e.  $>1$  nm, and higher sensitivity and higher duty cycles, i.e. larger field of views, thus collecting larger exposure times per point on the sky per day. Reaching larger fields of view is accomplished by either coded aperture imaging, a technique applied since the late 1970s and currently in wide use through for

instance BAT on Swift (Barthelmy et al. 2005) and ECLAIRs, time multiplexing, such as in MAXI, and Lobster eye optics, a technique applied since only since a few years through LEIA (Zhang et al. 2022) and WXT. Coded aperture imaging (Dicke 1968; Ables 1968) is a relatively simple and low-cost technique. Although it is less sensitive than direct focusing techniques by a few orders of magnitude, it is sensitive enough to detect many interesting transients in our own galaxy (e.g., accreting stellar black holes, thermonuclear flashes on neutron stars, stellar flares) and beyond (e.g., GRBs). This technique has, therefore, been very successful.

Coded aperture cameras (for reviews see, Caroli et al. 1987; in 't Zand 1992; Skinner 2008; Braga 2020; Goldwurm & Gros 2022) are usually based on a planar detector with identical spatial resolutions in both dimensions, yielding identical angular resolutions in those dimensions. This is a convenient setup. However, this is not strictly necessary. For example, the Super-AGILE instrument on the AGILE satellite (Feroci et al. 2010; Evangelista 2010) consisted of two pairs of identical cameras with each camera a high resolution in only one dimension and a coarse resolution in the other. By co-aligning both cameras to the same field of view but orthogonally with respect to each other, the 1D cameras accomplish a high angular resolution in both dimensions. This more involved setup was necessitated by the 1D nature of the silicon microstrip detectors but also has a number of advantages in terms of weight and power consump-

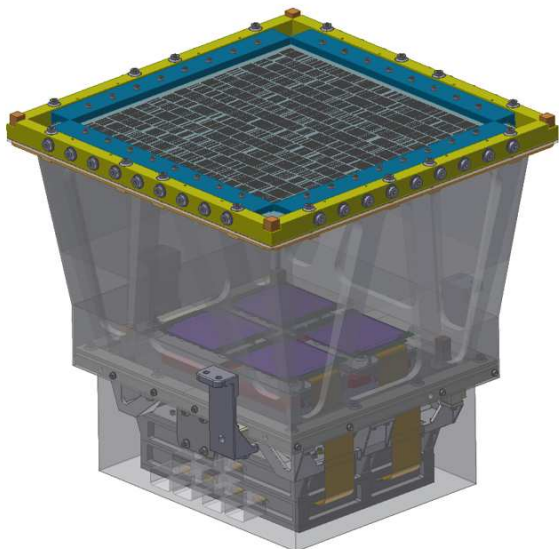


**Fig. 1.** WFM camera shown with the shielding being made slightly transparent. In purple, the 4 SDDs are depicted, on top the mask.

tion. The present paper is about an instrument concept similar to that of SuperAGILE but involving better performing silicon drift detectors (SDDs) and more pairs of orthogonal cameras to increase the field of view. It is called the Wide-Field Monitor (WFM). While other WFM publications focus on the hardware implementation of this instrument, we here focus on the principles of the software implementation: the development of an image and spectral reconstruction algorithm customized for the pair of coded aperture camera setup, the investigation of the performance with these algorithms and a comparison with a would-be 2D setup. This paper focuses on principles and first-order assessments of performance and as such is a state-of-the-art report. In the future, software development needs to continue and simulations need to reach a higher level of fidelity, ultimately culminating in analysis software for real data.

After introducing the WFM in more detail in Sect. 2, we summarize decoding algorithms in general and in particular for the WFM in Sect. 3. In Sect. 4, we explain how we approach the simulations of the sources, background and the instrument response. In Sect. 5, we discuss the simulation results of the images and what this says about the performance of the WFM, in Sect. 6 for the spectral simulations. We end in Sect. 7 with the conclusions of our study and the way forward with regards to the treatment of WFM data once the instrument flies.

## 2. The Wide Field Monitor

The concept of the Wide Field Monitor instrument was conceived 15 years ago and found a first application in the proposal for the Large Observatory For Timing (LOFT; Feroci et al. 2012; Brandt et al. 2014), followed by concept studies for the enhanced X-ray Timing and Polarimetry mission (eXTP; Zhang et al. 2019; Hernanz et al. 2018, 2022, 2024; Zwart et al. 2022), the Spectroscopic Time-Resolving Observatory for Broadband X-rays (STROBE-X; Ray et al. 2024; Remillard et al. 2024), the Astrophysics of Relativistic Compact Object mission (ARCO) submitted to the call for F3 mission concepts for ESA in 2025, and the Lunar Electromagnetic Monitor in X-rays (LEM-X; Del Monte et al. 2024). It is an array of wide-field cameras for

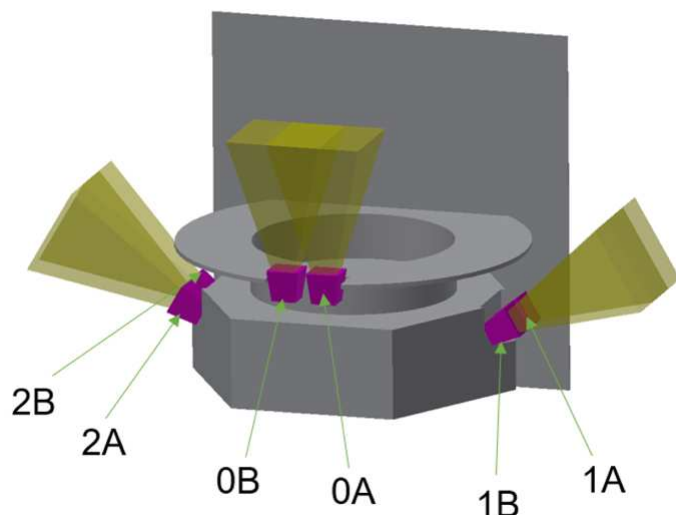


**Fig. 2.** Par example, a schematic of the WFM configuration foreseen for eXTP. The narrow-field instruments of eXTP are pointed upward, so WFM pair '0' covers the pointing of those instruments at the center of the field of view.

monitoring transient activity in the X-ray sky at photon energies between 2 and 50 keV. The field of view of each camera is 20% of the full sky and an array, therefore, enables exceptionally high duty cycle monitoring. The instrument consists basically of  $N$  pairs of orthogonal 1D coded aperture cameras. They are often referred to as 1.5D cameras because the SDDs have resolution, albeit coarse, in the perpendicular dimension (e.g., Hernanz et al. 2018). Table 1 summarizes the characteristics of one WFM camera as designed for eXTP. A prototype of such a camera is currently under construction at ICE-CSIC (Barcelona).

Each WFM camera hosts  $2 \times 2$  SDDs in one detector plane that have a high spatial resolution in one direction and a coarse resolution in the other (see Fig. 1). Each of the 4 detectors has a sensitive area of  $6.5 \times 7.0 \text{ cm}^2$ . The  $2 \times 2$  detector array is interspaced by 1.3 cm along the coarse direction and 2.8 cm along the fine direction. This space is a dead area in the detector plane. The detector plane has sensitivity within a  $15.8 \times 15.3 \text{ cm}^2$  boundary. A coded mask of size  $26.0 \times 26.0 \text{ cm}^2$  is 20.29 cm above the detector plane. The mask pattern consists of  $1040 \times 16$  elements of size  $0.025 \times 1.64 \text{ cm}^2$ , thus, after ignoring the first and last rib (see below) covering  $26.0 \times 26.0 \text{ cm}^2$  (here  $X$  is assumed along the fine direction and  $Y$  along the coarse). The space between mask and detector plane is shielded by a collimator to prevent photons from reaching the detector without passing through the mask. Each camera has a field of view of  $90 \times 90$  square degrees of which the central  $29 \times 29$  square degrees illuminate the full detector array (with part of the mask) and is (somewhat confusingly) called the 'fully coded' field of view. The optical design of the camera is basically unchanged since 2010 (e.g., Donnarumma et al. 2012; Brandt et al. 2014). To produce a setup with equal high angular resolution in both dimensions, each camera is paired with an identical camera rotated by 90 degrees along the optical axis. The ultimate WFM configuration consists of  $N$  pairs of cameras, each pointed at a

**Table 1.** Specifications of WFM relevant for imaging

Item	Parameter	Value
Mask	Physical size	260.0 mm $\times$ 260.0 mm $\times$ 0.15 mm
	Pattern	1040 $\times$ 16 elements of 0.25 $\times$ 16.4 mm <sup>2</sup> (the latter encompassing 2.4 mm ribs and 14.0 mm open areas)
Detector	Material	Tungsten 0.15 mm thick (<0.3% transparent for E<30 keV)
	Type	4 Silicon drift detectors in a 2 $\times$ 2 array each
	Size	77 mm $\times$ 72 mm $\times$ 0.45 mm each
	Boundary of combined sensitive area	158 $\times$ 153 mm <sup>2</sup>
	Quantum efficiency	>97% for E<10 keV, >33% for E<20 keV
Foil	Position resolution (FWHM)	<60 $\mu$ m along X and <8 mm along Y
	Energy resolution (FWHM)	< 300 eV at 6 keV
	Thickness multi-layer insulator above mask	12.70 $\mu$ m kapton + 0.10 $\mu$ m Al + 0.15 $\mu$ m SiO <sub>2</sub>
	Thickness micrometeorite protection	15 $\mu$ m polypropylene
Geometry	Mask-detector distance	203.05 mm (from top mask surface to top SDD surface)
	Field of view	90 $\times$ 90 square degrees (29 $\times$ 29 square degrees FCFOV)
Data	Angular resolution (FWHM, on axis)	fine 4.4 arcmin, coarse 4.6 deg
	Photon positions	on detector full resolution (unbinned)
	Time binning	10 $\mu$ s nominal
	Photon energy binning	1024 channels

different position on the sky. In LOFT, N=4, in eXTP N=3 (see Fig. 2), in STROBE-X N=4, in ARCO N=1 and in LEM-X N=7.

The mask pattern is based on a cyclic difference set from biquadratic residues of primes  $v = 4x^2 + 1$  with  $x$  odd (theorem 5.16 in Baumert 1971), see also Gottesman & Fenimore (1989), where set elements are  $j = \text{mod}(i^4, v)$  for  $i = 1..v$ . This yields that 25% of the numbers between 1 and  $v$  are a member. At those positions the mask pattern is defined to be open, at all the others closed. For the mask in the WFM,  $v$  was chosen to be 16901 ( $x = 65$ ). This mask pattern is folded in 2 dimensions over a 1040  $\times$  16 array of 0.25 mm  $\times$  16.4 mm elements with the last 261 members of the biquadratic residue set not used. The mask incorporates 2.4 mm closed ribs within the 16.4 mm long slits, so that the effective open area of the mask becomes 21.6%, see Fig. 3.

The WFM is, like all coded aperture cameras and perhaps even more so because of its  $2 \times 1.5D$  nature, an indirect imaging instrument. In contrast to focusing telescopes, the signal of all cosmic sources is coded and mixed which gives rise to the disadvantage that there is cross talk between sources and decreased sensitivity for the same photon-collecting area. An essential ingredient of a coded aperture camera is the algorithm to decode the signal from the coded detector domain to the decoded sky domain. The purpose of the present paper is to discuss methods to treat the data through such algorithms and verify through detailed simulations the expected performance.

### 3. Algorithms to decode detector data to sky data

The literature discusses various successful algorithms to accomplish reconstruction of sky data from coded aperture detector data (e.g., Rideout 1995). This includes cross correlation (Brown 1974; Fenimore & Cannon 1978), the maximum likelihood method (MLM; Skinner & Nottingham 1993; Nottingham 1993), the maximum entropy method (Willingale 1981), Wiener filtering (Sims et al. 1980; Rideout & Skinner 1996) and machine-learning techniques (Meißner et al. 2023). The cross correlation method has been extended with iterative removal of sources (IROS Hammersley 1986; Hammersley et al. 1992; in 't Zand 1992), fine sampling and delta decoding (Fenimore & Cannon 1981). We here develop the methods of

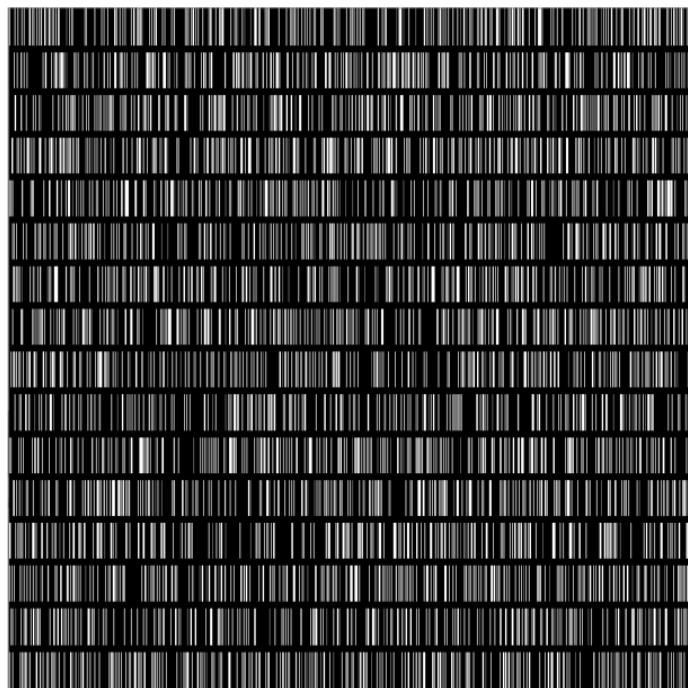


**Fig. 3.** WFM mask. The cyclic difference set is laid down starting from the bottom left, going first from left to right and then bottom to top.

IROS and MLM for application in WFM. These methods have different purposes. IROS excels in fast sky image reconstruction and search for previously unknown point sources. MLM excels in the best determination of fluxes and positions. IROS provides a map of the complete field of view by the fast cross correlation technique using FFTs. MLM can provide a sky map by calculating detector images for every possible sky location which is a slower process. Our approach to data handling of WFM data is to first find all point sources through IROS and then characterize all those point sources (i.e., determine positions, light curves and spectra) through MLM.

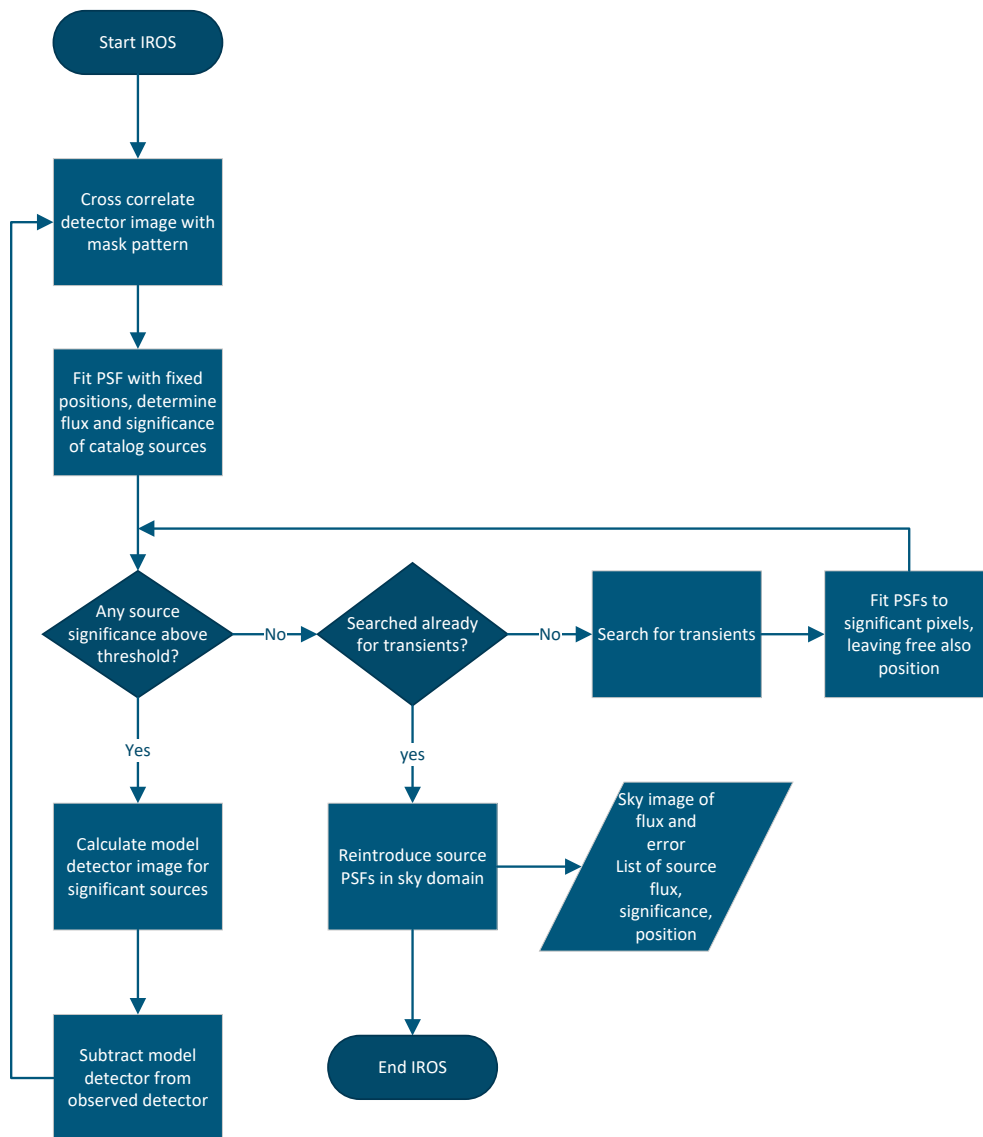


**Fig. 4.** Flow diagram of IROS.

### 3.1. Iterative Removal of Sources

#### 3.1.1. Outline

IROS is an analogue of the ‘clean’ algorithm in interferometric radio-astronomy imaging (Högbom 1974). The basis of IROS (Hammersley 1986) is a cross correlation of the detector image with a mathematical version of the mask pattern that ensures that the expected flux at any pixel where there is no source is zero and is properly normalized to  $\text{phot s}^{-1} \text{cm}^{-2}$  for any source pixel. The geometrical response of the instrument needs to be taken into account to properly normalize by  $\text{cm}^2$ , for instance obscuration by support structures of the detector or mask. Any photon energy-dependent response parameters of the instrument, such as detector spatial resolution, mask transparency and shadowing need to be taken into account through for instance modeling of the point spread function in the sky and detector domains.

A typical feature of cross correlation images is ‘coding noise’. Mask patterns are chosen such that their autocorrelation is a delta function (Palmieri 1974; Fenimore & Cannon 1978). This requires the application of patterns based on pseudo-

random arrays, such as cyclic difference sets, and the proper lay-down in two dimensions. Figure 3 shows the mask pattern of the WFM envisaged for eXTP. Even with a pseudo-random pattern, the autocorrelation is only 2-valued if the full pattern is involved in coding any sky position. There are some camera configurations where this is accomplished, for instance by applying a repeated ideal mask pattern and putting a collimator on the detector that limits the field of view from any position on the detector to one complete cycle of such a pattern (Hammersley 1986). However, in many practical applications (e.g., when sensitivity or field of view is critical) this is not the case and coding noise is present, with a variance that is proportional to the portion of the basic pattern not used in coding a sky position. This also pertains to the WFM. The mask pattern is larger than the detector, so is never completely recorded. One calls the portion of the field of view that uses the complete detector the ‘fully coded field of view’ (FCFOV). However, in the WFM this is actually not coded with the complete mask pattern so has coding noise. Outside the FCFOV only part of the detector is illuminated and the coding noise becomes worse, although smaller than for a random mask pattern. Generally speaking, the local coding noise stan-

standard deviation will be a fraction of the random case that is equal to the square root of the fraction of the mask pattern employed in coding that locality. Ergo, we expect the base level of coding noise standard deviation to be  $\sqrt{1 - N_{\text{SDD}} A_{\text{SDD}} / A_{\text{mask}}} = 0.85$  of that for a random mask pattern, with  $N_{\text{SDD}} = 4$  the number of SDDs, the  $A_{\text{SDD}} = 6.5 \times 7.0 \text{ cm}^2$  the sensitive area per SDD and  $A_{\text{mask}} = 26.0 \times 26.0 \text{ cm}^2$  the area of the mask. The expression under the square root represents the minimum fraction of the complete mask pattern not used during the coding of a sky source. Coding noise is a systematic and deterministic noise, meaning that it does not diminish with exposure time as opposed to statistical noise. However, one can eliminate or minimize it with IROS.

IROS entails the following critical steps (see also Fig. 4):

1. cross correlate the detector image with a mathematical version of the mask pattern to a sky image, properly normalized that each pixel has  $\text{phot s}^{-1} \text{ cm}^{-2}$  as unit, and an accompanying error image of the statistical standard deviation in each pixel based on Poisson photon count statistics (see, e.g., in 't Zand 1992);
2. identify significantly detected point sources in the cross correlation image where significance is determined with respect to the local image standard deviation after a PSF fit that yields their fluxes (e.g., in 't Zand et al. 1994);
3. model the detector image for these point sources and exposure time;
4. subtract the model detector image from the observed detector image;
5. cross correlate the residual detector image to a sky image. The sky image will still have systematic biases because the initial flux determination is subject to coding noise, but the coding noise will be smaller than after the previous iteration;
6. go back to step 2 while preserving the original error image and iterate until there are no more significant point sources remaining;
7. add up the PSF models of all iterations and sources back in the last cross correlation image and perform a PSF fit to determine the best-estimate fluxes.

The convergence of the iterative process of IROS can be significantly improved if one takes into account the knowledge about known point sources in the field of view, in other words uses an X-ray catalog and the accurate pointing direction of the camera (usually provided by optical star trackers on board). After all, the known point sources concern the brightest sources, except for an incidental new transient, and are the dominant source of coding noise. Furthermore, one can keep the positions of these frozen during the PSF fits. Freezing the positions of the bright sources leaves less parameters to fit and eases the iteration process, particularly in crowded fields (likely in wide-field applications) because the coding noise can become large. If there is no pointing information available or its accuracy is compromised, the camera's X-ray data can be used for plate solving constellations of X-ray stars and pointing information can be recovered.

In IROS, we chose to fit the model to the data in the sky domain. Alternatively, one could do this in the detector domain, but in principle this does not matter as translation of detector data to sky data is the cross correlation procedure which is a linear combination of detector data into sky data that is independent for every sky pixel.

### 3.1.2. Implementation

Our implementation of IROS for the WFM has the following specifics.

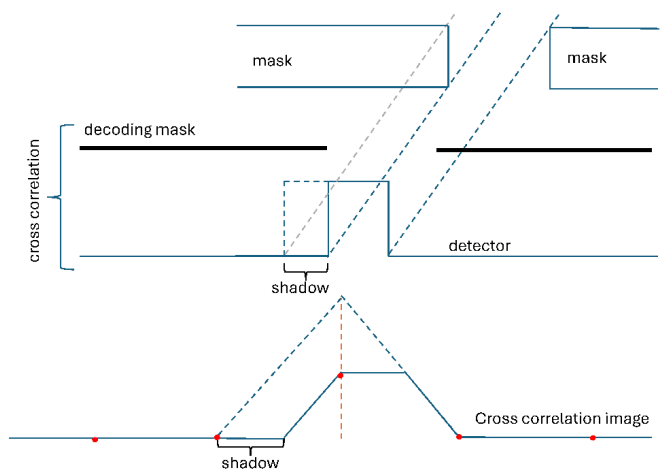


**Fig. 5.** PSF formation along the 'fine' direction. In the top section of the figure, the rays of an off-axis source illuminate the thick mask somewhat sideways and introduce a shadow on one side of the projection of the mask element on the detector (middle blue graph). When cross correlating with the decoding mask (moving the decoding mask from left to right over the detector, see middle blue graph), this introduces (bottom blue graph) 1) a flat top to the PSF which is off centered; 2) a lower PSF peak representative of less sensitive area and 3) a narrower PSF. The red dots indicate where the discrete cross correlation would sample the PSF if the sampling is equal to the mask element size. The sampled cross correlation looks like there is no shadowing but its integral is actually smaller.

- The WFM data is event-by-event and include positions with a readout accuracy that is fraction of the  $60 \mu\text{m}$  fine resolution. We here choose to bin these data to detector bins of  $0.25 \text{ mm} \times 0.25 \text{ mm}$ , commensurate with the fine mask element size, yielding a total detector image size of  $632 \times 632$  pixels (filling up dead areas between SDDs or along their edges with zeros to obtain paired detector images for X and Y cameras) and a sky image size of  $1671 \times 1671$  pixels.
- The cross correlation images of the X and Y cameras are added in step 1, resulting in a cross-like PSF which is fitted to simultaneously obtain accurate estimates for locations in X as well as Y and flux in step 2, while the treatment of the detector images of X and Y in steps 3 and 4 remain separate. Thus, uncertainty about the coarse position of each source can be avoided and the iterative process is more efficient.
- If, in step 3, the center of the PSF of one source is on the PSF of another source, only the most significant source will be included in the current iteration. In a next iteration, the ignored source will likely be the most significant one.
- If a source has been 'subtracted' in a previous iteration, negative fluxes are allowed to be subtracted if they are significant. This corrects possible over-estimates of the flux in a previous iteration (due to a higher coding noise).
- The PSF looks like in Fig. 5. Due the shadowing by the mask thickness ( $150 \mu\text{m}$ ) for an off-axis source, the PSF particularly along the fine direction has a plateau that depends on the off-axis angle and is off-centered. Since we have chosen to use  $0.25 \text{ mm} \times 0.25 \text{ mm}$ , there is no oversampling which in principle introduces ambiguity in source positions, but this will be avoided by fixing the point source locations except for unknown sources and oversampling in MLM to accurately determine the position of new sources.

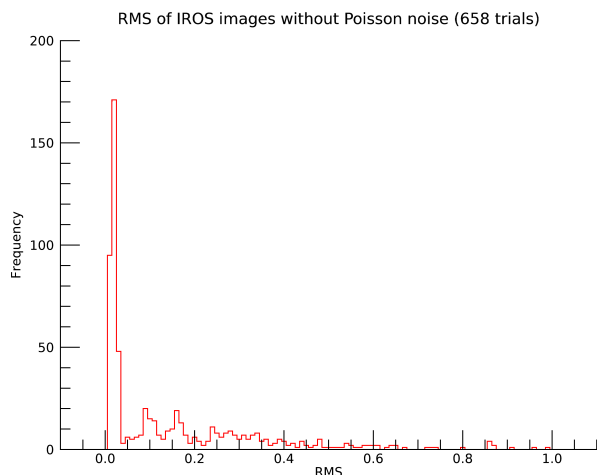


**Fig. 6.** Histogram of standard deviation values of significance images of the Galactic Center field solution without Poisson noise, for 658 different pointings (i.e., rotating from 0 to 359 deg in steps of 1 deg and for stepping diagonally over the image in 299 steps at one rotation angle).

It is noted that IROS can be run independently on the X or the Y camera. The sensitivity will decrease by  $\sqrt{2}$  and the source confusion will increase along the coarse direction, but a high level of redundancy is preserved. Similar for the multiple detectors in one detector plane.

### 3.1.3. Verification

One step in IROS is the calculation of the model detector image for a given source configuration (step 3). This is done through a geometric calculation of the projection of the mask on the discretized detector. This analytical step enables to verify the self-consistency of IROS: what one puts in should come out. This implies that source fluxes should be reproduced exactly and the standard deviation of any reconstructed sky image after source subtraction should be zero since no count statistics are involved. We have first tested this with just a single point source and then in the most complicated sky configuration possible namely that of the Galactic Center (GC) field.

The test for the single point source was done in various positions in the field of view and was every time ideal (standard deviation zero). For the Galactic Center field this is not the case. We find that IROS is able to diminish the standard deviation of the full significance image without point sources to generally 1–10% of the value that would be expected from Poisson noise for a 10 msec exposure, or equivalent to the Poisson noise for a 1 Msec exposure of the Galactic Center. Figure 6 shows the results in terms of standard deviation of significance images for 658 different observation pointing realizations.

## 3.2. Maximum Likelihood Method

### 3.2.1. Outline

Once all sources of detector events have been identified, in other words once all point and extended sources have been localized and the backgrounds calibrated, it may become desirable to apply further diagnostics on the sources: determine the time history of the fluxes (i.e., determine the light curves) and measure the

spectrum, if need be as a function of time or phase. This implies determination of source fluxes at many times and photon energies. In principle one can run IROS for every time and energy bin keeping source positions fixed, but this will require many computations and long processing times. Basically, this is because with IROS the flux is calculated in each of the almost 3 million sky pixels (in our WFM application) while one only needs the flux for around 100 sources. Therefore, one should resort to a method that is better suited and that method is MLM.

In MLM, the measured detector image  $D_i$  (in units of event counts per detector bin) for a given measured energy band is compared to a theoretical model consisting of a background component (or multiple background components, not considered here) and a combination of  $N_{\text{src}}$  point sources at different sky locations, all with free scale factors and taking into account the Poissonian nature of the counting process. Optimizing these scale factors by maximizing the likelihood  $\mathcal{L}$  gives the source strengths and associated uncertainties of the involved sources as well as an estimate for the background plus its uncertainty. In detail, for detector bin  $i$  we can write the expectation value  $E_i$  as:

$$E_i = \beta \cdot B_i + \sum_j S_j \cdot M_{ij} \quad (1)$$

where  $M_{ij}$  is the point-spread function at that detector bin  $i$  for source  $j$ ,  $S_j$  the source flux in sky bin  $j$ ,  $B_i$  the background image in detector bin  $i$  and  $\beta$  the scale factor of the total background component. The likelihood  $\mathcal{L}$ , taking into account the Poisson statistics, is defined as:

$$\mathcal{L} = \prod_i \frac{E_i^{D_i} \cdot \exp(-E_i)}{D_i!} \quad (2)$$

Assuming for simplicity that we are dealing with one source and one constant background model  $B_i$ , ignoring times when the Earth eclipses part of the field of view, we consider two hypotheses: a) the zero hypothesis  $\mathcal{H}_0$  stating that the data are described by background only i.e.  $E^{\mathcal{H}_0}(\beta) = \beta$ , and we have:

$$\mathcal{L}^{\mathcal{H}_0}(\beta) = \prod_i \frac{\beta^{D_i} \cdot \exp(-\beta)}{D_i!} \quad (3)$$

and b) the alternative hypothesis  $\mathcal{H}_1$  stating that the data are described in terms of a constant background and a point-source i.e.  $E^{\mathcal{H}_1}(\beta, S_1) = \beta + S_1 \cdot M_{i1}$ , resulting in:

$$\mathcal{L}^{\mathcal{H}_1}(\beta, S_1) = \prod_i \frac{(\beta + S_1 \cdot M_{i1})^{D_i} \cdot \exp(-\beta - S_1 \cdot M_{i1})}{D_i!} \quad (4)$$

Maximizing the natural logarithm of  $\mathcal{L}^{\mathcal{H}_1}(\beta, S_1)$  with respect to  $\beta$  and  $S_1$ , and the natural logarithm of  $\mathcal{L}^{\mathcal{H}_0}(\beta)$  with respect to  $\beta$ , we can define the maximum likelihood ratio (MLR)  $Q$  as

$$Q = -2 \cdot \ln \left( \frac{\mathcal{L}^{\mathcal{H}_0^{\max}}(\beta)}{\mathcal{L}^{\mathcal{H}_1^{\max}}(\beta, S_1)} \right) \quad (5)$$

This (test) statistic is successfully used in high-energy astrophysics, particularly in the gamma-ray domain, for parameter optimization and hypothesis testing. More information on the basic principles, the method and caveats can be found in Wilks

(1938), Eadie et al. (1971) and Cash (1979), while its application to high-energy data analysis procedures is described in detail in Pollock et al. (1981), Mattox et al. (1996), de Boer et al. (1992) and Abdo et al. (2009) for COS-B, CGRO-EGRET, CGRO-COMPTEL and Fermi-LAT, respectively. An application of the method to BeppoSAX X-ray data is given in in 't Zand et al. (2000).

In our case the quantity  $Q$  is distributed as  $\chi^2$  for one degree of freedom under proper conditions. Therefore, at known source locations (e.g., from source catalogues)  $Q$  values of 9, 16, 25,... correspond to 3, 4, 5, ...  $\sigma$  detection significances.

If we do not know a priori the location of a source we can scan the sky on a grid by assuming a source location at each grid point and evaluating the quantity  $Q$  and so constituting a map - the MLR significance map. To assess the significance of prominent new-source features in the MLR-map we have to take into account the number of trials i.e. the number of independent spatial resolution elements ( $\sim 4' \times 4'$ ) searched for in the map, which degrades the detection significance compared to the assumption of the one degree of freedom significance at the particular location. The construction of this map is a tedious and CPU-time consuming process given the non-linear nature of the optimization procedure and the many scan locations (preferentially sampled at step sizes smaller than the angular resolution of the camera) involved to build the map requiring each time a different detector model. This procedure is feasible as long it is limited to a small region around a new source for the sake of its identification, but the computations quickly become unsustainable for a large field of view (Appendix A shows an example of a sub-region of the WFM field of view).

### 3.2.2. Implementation

The practical implementation is as follows. At first, the events in the detector plane (for a measured energy band) are binned in  $30 \mu\text{m}$  by  $3.5 \text{ mm}$  detector pixels along the fine and coarse directions, respectively, which is sufficiently small to sample sufficiently dense the distribution given the  $60 \mu\text{m}$  and  $8 \text{ mm}$  FWHM resolution in fine- and coarse directions of the detector. This results in a  $2170 \times 20$  binning mesh per detector plane given its (X,Y) sizes. This detector image is denoted by  $D_i$ .

The next step is to accurately determine the pixel illumination factor (PIF) for each pixel in the detector plane for a given source scan direction. For this purpose we subdivide each detector pixel in  $M \times M$  elements to boost the detector image resolution, and determine whether the (centers of) these elements are blocked by a mask element or not when back projecting to that source in the sky.  $M$  is typically 3. We perform this procedure for both the upper and lower mask plane (the mask has a thickness of  $150 \mu\text{m}$ ). The current implementation yields a 1 or 0 for an open and blocked element, respectively. In principle the method can include energy-dependent absorption effects (the mask is more opaque at lower X-ray energies) by the Tungsten mask elements using the measured energy of the events as a proxy for the photon energy, yielding fractional values between 0 and 1.

We also take into account the averaged penetration depth  $d_{\text{pen}}$  of the photons in the silicon detector material, making effectively the detector-mask distance larger by  $d_{\text{pen}}$ . Finally, we blur through convolution of the detector image, as derived above for the case in which we exactly know the (X,Y)-location of the absorbed photon in the detector plane, with a 2D-distribution that accurately describes the blurring of the charge cloud reconstruction produced by the absorbed photon. This description is a 'modified' sech(x) function (secans hyperbolicus) of the form

$$\text{modsech}(x|\mathbf{a}) = \frac{a_0}{\cosh\left(\left(1 + \frac{x-a_1}{a_2}\right)^{a_3}\right)}, \quad (6)$$

where  $x$  is the spatial dependence and  $\mathbf{a}$  a 4-element parameter array describing the model PSF. Only the 'shape' parameters,  $a_2$  and  $a_3$ , are relevant for the normalized distribution used in the convolution process.

Thus, we are equipped with the necessary elements, a) the measured detector  $D_i$ , b) the point spread function  $M_{ij}$  for a source at the scan-location and c) a background estimate assumed to be homogeneous for isotropic diffuse emission, to calculate the maximum likelihood ratio  $Q_k$  for each scan location  $k$ . The square root of this number yields the significance image.

Due to the additive nature of  $\ln\mathcal{L}$  (i.e., the multiplicative character of the likelihood  $\mathcal{L}$ ) the method can easily be extended to analyze an orthogonal camera pair assuming that both components are identical and operate simultaneously under similar observation conditions. In that case we can assume that the same fit (scale) parameters for the models hold for each component of the camera pair. In practice one should correct for possible slightly different exposure times and misalignments of each camera.

## 4. Simulation approach

### 4.1. Simulation of sky

Our baseline for the simulation of point sources is the catalog of cosmic X-ray point sources as compiled from observations with the RossiXTE All-Sky Monitor (Levine et al. 1996, 2006, 2011) and BeppoSAX-WFC (Jager et al. 1997). This includes 1.5-12 keV photon fluxes of those point sources averaged over the 16 year lifetime of the RossiXTE mission (1996-2012), the best-known positions, often from optical or radio observations, and average spectra measured with BeppoSAX-WFC (Verrecchia et al. 2007). The fluxes were normalized to the flux of the Crab and then multiplied with the calculated photon flux of the Crab expected in the WFM in the bandpass of 2 to 30 keV ( $2.4 \text{ phot s}^{-1} \text{ cm}^{-2}$ ; based on the Crab spectral model of Kirsch et al. 2005). It is noted that this is an educated estimate of those fluxes with an estimated accuracy of a few tens of percents, but this is enough for our purposes to assess the WFM imaging capability and sensitivity.

We simulate the sky background by a calculation of the detector response to an isotropic background. This local response of the detector depends on the field of view as seen from that position on the detector since the field of view can be modulated by shadowing by any mechanical structure above it, including the mask. Our simulation entails a calculation of that field of view and a scaling that is determined from a Monte Carlo simulation of the cosmic diffuse X-ray background (CXB) which is  $215 \text{ phot s}^{-1} \text{ cam}^{-1}$  for the full bandpass, which is in line with CXB model in Marshall et al. (1980). Apart from the sky background, real observations will also include particle-induced background (Campana et al. 2012) and the Galactic Ridge emission (Valinia & Marshall 1998). However, the photon rate of these contributions are expected to be less than 10% of the CXB, so negligible at the current level of fidelity.

We employ two sky fields as test cases:

1. Faint field, pointed at the Large Magellanic Cloud, in particular the point source LMC X-1. The combined photon count rate of all point sources is smaller than the background. The typical flux of a bright source in this FOV is a few tens of mCrabs. The brightest object is Cen X-3 at 53 mCrab at

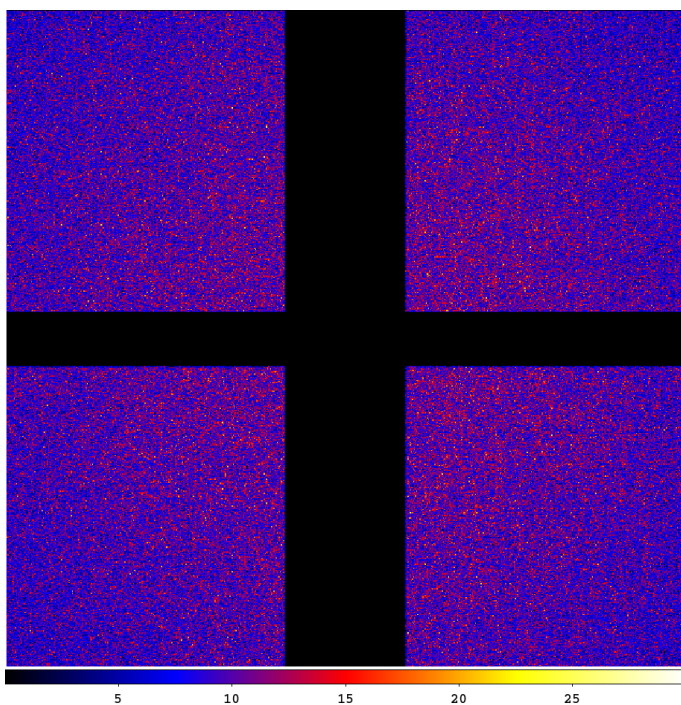


**Fig. 7.** Image of X detector (fine resolution along X) for LMC field for an observation with an exposure time of 10 ks. Unit is photon counts per  $0.25 \text{ mm} \times 0.25 \text{ mm}$  bin. The color scale bar of the pixel values is shown at the bottom. The cross is due to the spaces between the four SDD tiles in the detector plane.

an off-axis angle of  $34^\circ$ . The CXB count rate encompasses 97.6% of the total and so dominates.

- Bright field, pointed at the Galactic Center. The combined photon count rate of point sources far exceeds that of the background. In particular, this field contains Sco X-1 at an off-axis angle of  $24^\circ$ ,  $10^\circ$  outside the fully coded FOV. The average count rate of Sco X-1 is 11 times higher than the next brightest source in the field, GX 5-1, which is at an off-axis angle of  $5^\circ$ . This field is an excellent test of systematic errors in the reconstruction. The CXB count rate encompasses 19.7% of the total and, therefore, is of secondary magnitude.

#### 4.2. Simulation of detector response

Simulations of the WFM detector response are calculated per (array of) cameras with the physics-based software tool 'WFM Imaging Simulation Environment for Montecarlo and ANalytical modeling' (WISEMAN). This tool is comprehensively described in Ceraudo et al. (2024). We here summarize.

##### 4.2.1. The simulation process

Photons from astrophysical sources (hereafter, primary photons) are generated in the field of view of the camera starting from the ASM catalog of X-ray point sources and the diffuse emission of the CXB. Extended sources such as the Galactic Ridge, supernova remnants and galaxy clusters are not included. Primary photons (tagged with celestial coordinates, photon energy and time of arrival) are projected uniformly on the top surface of the camera, and their direction is converted to the local frame of reference.

The first loss of primary photons flux occurs above the mask, where the presence of the Multi-Layer Insulator (MLI) foil is

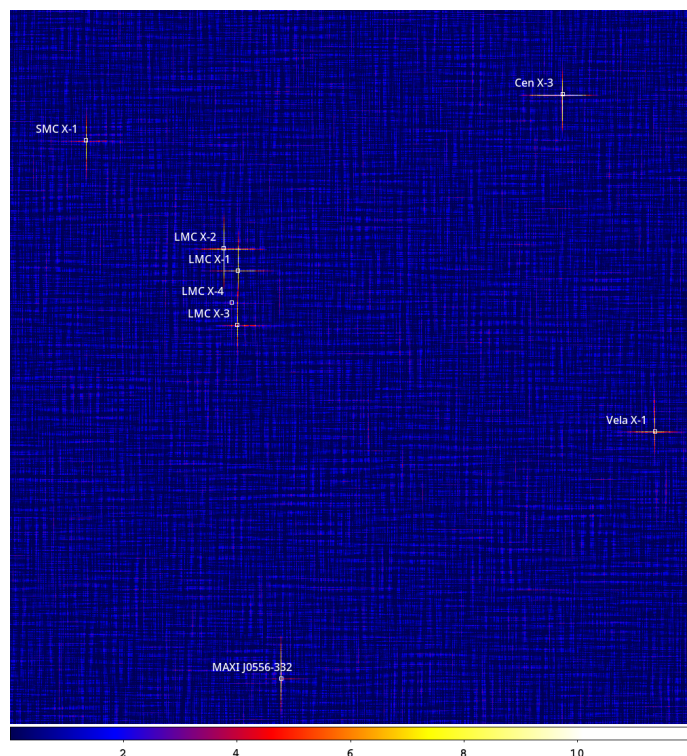


**Fig. 8.** Part of the sky image of the LMC observation as obtained through IROS, between  $-28^\circ$  and  $+40^\circ$  in the local frame along X and  $-39^\circ$  and  $+25^\circ$  in Y, zooming in on 54% of the total image showing the strongest sources in the field of view. The pixel unit is significance. Only sources brighter than 13 mCrab are labeled. The cross-like PSF of a source is not always apparent because its narrowness does not show well at this image reproduction; it is clearer when zooming in the pdf version of this paper.

simulated, with the photons surviving the passage according to a stochastic process based on the overall transparency of the MLI. Afterward, the trajectory of each photon is traced through the coded mask and the path into each (portion of) closed element is recorded, so that the transmission of each photon may be calculated via a random process. All surviving photons are then traced to the detector plane, via a polypropylene foil between mask and detector plane, and only those whose trajectories intersect with the detectors are followed further.

If the photon survives the passage through the inert layers of the top of the sensor, the interaction of a photon with the sensitive bulk is evaluated according to its energy and the path it actually traces, which depends on its direction of approach. If the photon is absorbed via photo-electric effect in the sensor, its energy is modified by the Fano noise in silicon, and then the drift of the liberated electrons is simulated. During the drift, the initially point-like charge cloud expands under the effect of diffusion, so that the charge  $\psi_i$  collected by an anode in position  $x_i$  is

$$\psi_i = \frac{1}{2} E \left[ \operatorname{erf} \left( \frac{x_i + p/2 - X}{\sigma \sqrt{2}} \right) - \operatorname{erf} \left( \frac{x_i - p/2 - X}{\sigma \sqrt{2}} \right) \right], \quad (7)$$

where  $p$  is the anode pitch ( $169 \mu\text{m}$ ),  $X$  and  $Y$  are the coordinates of the interaction of the photon with the detector,  $E$  its energy, and  $\sigma$  is the width of the charge distribution due to diffusion, expressed by

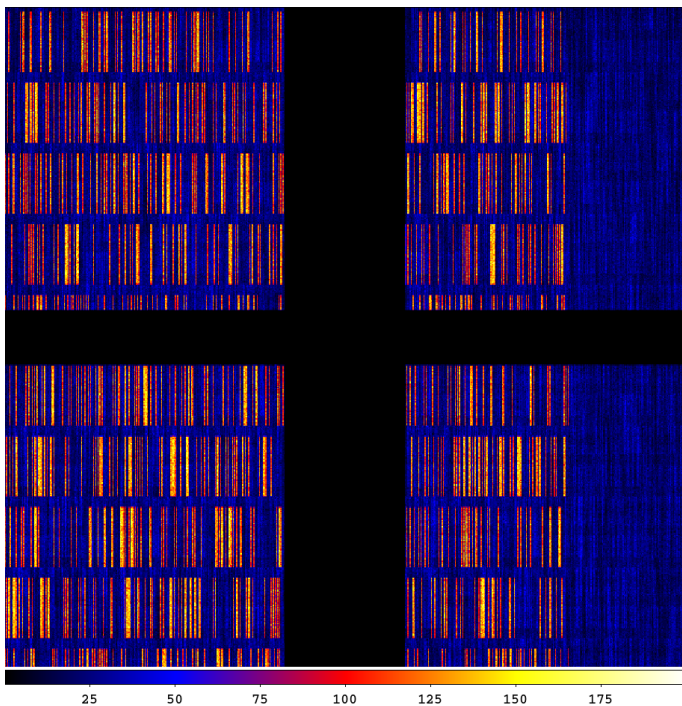


**Fig. 9.** Image of X detector for an observation of 10 ks exposure of GC field. The illumination by Sco X-1 is obvious. Unit is photon counts per  $0.25 \text{ mm} \times 0.25 \text{ mm}$  bin.

$$\sigma = \sqrt{2Dt + \sigma_0^2} = \sqrt{2 \frac{k_B T}{q} \mu \frac{Y}{\mu \epsilon} + \sigma_0^2} = \sqrt{2Y \frac{k_B T}{q \epsilon} + \sigma_0^2}, \quad (8)$$

with  $D$  the diffusion coefficient,  $t$  the drift time,  $\sigma_0$  the initial width of the charge cloud,  $T$  the detector temperature,  $\mu$  the electron mobility,  $\epsilon$  the electric field,  $q$  the elementary charge and  $k_B$  Boltzmann's constant (Campana et al. 2011).

Readout is implemented by adding noise to each anode reading, converting the continuous energy values to the integer units of the analog-to-digital converter and adding channel-wise offsets as well as an event-dependent baseline.

The final step of the simulation essentially consists of estimating the parameters of the interacting photon ( $X$ ,  $Y$  and  $E$ ) from the recorded list of digitized anode readings. This procedure involves the application of user-provided calibration tables (e.g., gain, offset etc.) as well as a fit of the recorded charge profile.

At the end of the simulation, an output file resembling the actual data stream of an operating instrument is provided, featuring the list of the inferred energies and impact ( $X, Y$ ) positions of the photons.

#### 4.2.2. Strengths and limitations

The WISEMAN simulator can be employed to estimate the scientific performances of an arbitrary arrangement of WFM cameras, hence it is not limited to a specific configuration (e.g., LOFT, eXTP, STROBE-X, ARCO or LEM-X). Moreover, since nearly every camera subsystem is implemented, parametric simulations can be performed to perfect the design as a function of geometry, building materials and general characteristics and performances of the various components (e.g. electronic noise, defective readout channels).

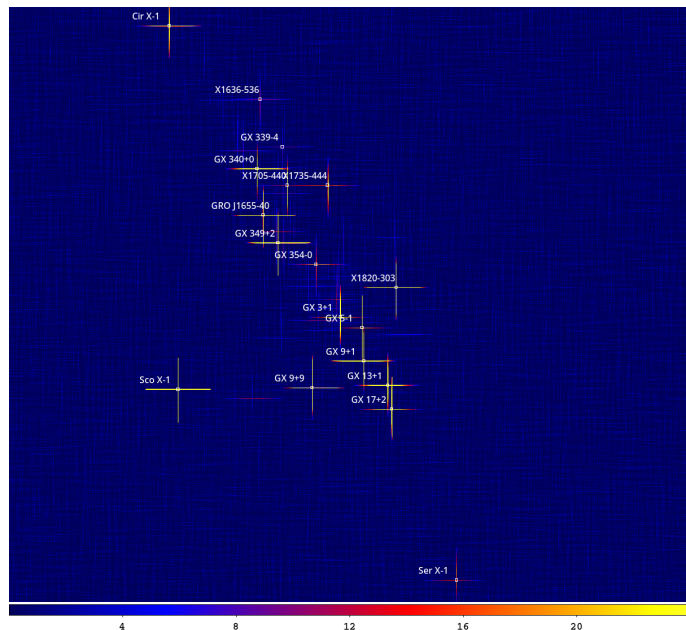


**Fig. 10.** Part of the sky image of the GC observation as obtained through IROS, between  $-44^\circ$  and  $+45^\circ$  in the local frame along  $X$  and  $-35^\circ$  and  $+35^\circ$  in  $Y$ , zooming in on 30% of the total image showing the strongest sources in the field of view. The pixel unit is significance. Only sources brighter than 80 mCrab are labeled. The cross-like PSF of a source is not always apparent because its narrowness does not show well at this image reproduction; it is clearer when zooming in the pdf version of this paper.

Deviations from the ideal geometric configuration may also be investigated, since each subsystem may be freely positioned around its baseline location, allowing to simulate three-dimensional shifts and rotations of mask and detectors, and therefore their impact on the scientific performances of the instrument. Likewise, the sensitivity of the reconstruction algorithms to deviations from the baseline configurations that are unaccounted for may be assessed in this way.

At the current stage of development, the simulator features some limitations. For example, all primary photons (and associated detected events) are treated completely independently from each another, implying the impossibility to quantify such effects as pile up and dead time although that is expected to be limited. Additionally, only photons from astrophysical sources are simulated and their energy and direction stay constant until the final interaction with the detector: no particle background or particle-induced photon background are implemented, and primaries are not reprocessed via scattering. Likewise, events deriving from electronic noise are not considered. Finally, as previously mentioned, the astrophysical photons sources are currently limited to point sources, provided via a catalog, and the CXB. No Galactic Ridge has been included so far.

Also, at the current stage of development, the model that is used for simulating input for the IROS tests assumes infinitely dense masks and detectors and real photon absorption positions. The algorithm to derive photon detector positions is not developed yet at a sufficiently high fidelity to avoid large-scale low-amplitude features in detector images that are noticeable in IROS images. For the MLM simulations, the model is sufficient and avoids these idealizations, because the focus there is on (spectra of) bright sources.

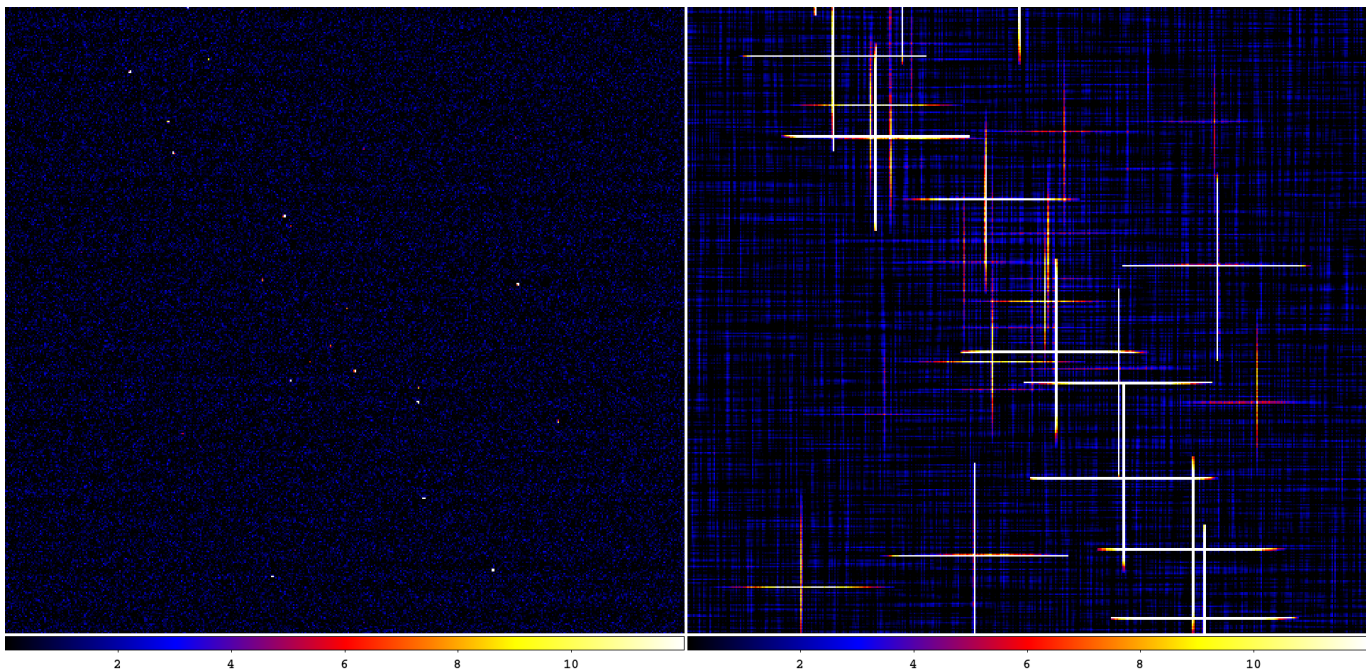


**Fig. 11.** Comparison of sky reconstructions of the Galactic Center field between the  $2 \times 1.5D$  configuration (right) and the  $1 \times 2D$  configuration (left), zooming in on central quarter of the field of view.

## 5. Image simulations

### 5.1. IROS on LMC field

The detector image of the WFM X camera of the simulated 10 ksec observation on the LMC is shown in Fig. 7. This simulation involves 2.7 million photons. It shows the following features:

- a thick vertical center bar running and a thin horizontal one. This aligns with the spaces between the 4 SDDs. The space is larger in X because there is more hardware along those edges of the SDDs;
- no obvious exposures of point sources, because their count rates are negligible with respect to that of the CXB;
- a large-scale non-uniformity peaking at the center of the detector. This is due to the field of view as seen from the center of the detector being approximately 20% larger than from the corners.

The Y camera shows a similar detector image (not shown) but rotated by  $90^\circ$ .

The IROS solution of this observation is shown in Fig. 8, zooming in to 41% of the total image with the 6 most significant sources. The weakest source is LMC X-4 (not shown) at a significance of 3.1, suggesting a 5-sigma detection limit of 7 mCrab for this field.

### 5.2. IROS on GC field

Figure 9 shows the detector image of the X camera for the 10 ksec simulated observation of the Galactic Center. This measurement with the X camera includes 11 million photons, 21% from the CXB and 44% from Sco X-1 – the brightest point source in the field of view. The Y camera image (not shown) is similar. Many of the 163 catalog sources in the field of view leave photons on the detector.

This observation is in juxtaposition to the one on the LMC. It is dominated by the brightest point sources and as such represents the least sensitive field in the sky. This is clear from the detector image which is dominated by the illumination by Sco X-

1 at an off axis angle of  $24^\circ$ . This illumination also clearly shows a shadowgram of the coded mask with the 14 mm long mask elements and the 2.4 mm ribs between them along the same axis. The CXB is not discernable, as opposed to the image of the LMC field (Fig. 7).

In Fig. 10, the IROS solution is shown for this observation. This 10 ksec observation reveals detections of 41 point sources. IROS is effective in that it brings down the overall standard deviation in the significance image down from 28 to 1.1, the large initial standard deviation being due to coding noise from mostly Sco X-1. After the first IROS iteration, involving only the subtraction of Sco X-1, the standard deviation already goes down to 6. The significance of Sco X-1 is very high at about 1400. The significance of a source very close to the Galactic center, 1E1747.0-2942, is 2.3. This translates to a 5-sigma sensitivity of 25 mCrab, roughly 3 times less sensitive than the faint LMC field which, therefore, shows the dynamic range of sensitivities for any WFM observation within the same exposure time.

Sco X-1 is  $24^\circ$  from the Galactic Center. With a single camera pair field of view of  $90 \times 90$  square degrees it is cumbersome to keep Sco X-1 outside the field of view while keeping focused on the Galactic Center. It would imply that the Galactic Center needed to be placed some 25 degrees from the edge of the field of view, or 20-30 degrees from the center, depending whether it would be moved towards a corner or not. Since the FCFOV is the central  $29 \times 29$  square degrees part of the camera field, the loss in detector area covering the Galactic Center would be limited to 15-30%.

The detrimental effect of Sco X-1 on the sensitivity was calculated by doing the same GC simulation while ‘turning off’ Sco X-1. This shows a 40% improvement in the sensitivity of the 10 ksec GC observation for the on-axis position and less for far away from Sco X-1. Because Sco X-1 is outside the FCFOV, there are parts in the sky image opposite to where Sco X-1 resides that are not affected by the presence of Sco X-1, but the vast majority of the Galactic Bulge sources are within reach of the Sco X-1 cross talk.

In Appendix B we show, as illustration, a simulation of a complete WFM instrument for the eXTP configuration ( $N=3$ ).

### 5.3. Special test: imaging with $1 \times 2D$ instead of $2 \times 1.5D$

In order to assess how the WFM  $2 \times 1.5D$  configuration compares to a  $1 \times 2D$  configuration with similar capabilities, we set up a simulation with a 2D camera that has twice the detector area, but identical field of view and angular resolution as the  $2 \times 1.5D$  configuration. This implies a simple scaling of all linear sizes by a factor of  $\sqrt{2}$ . The result is shown in Fig. 11. Essentially, the significances of all sources are similar as are the positional uncertainties for non-cataloged sources, but the source confusion in the  $2 \times 1.5D$  configuration is substantially worse if two sources are located on each other's PSF cross which extends over a  $\sim 256$  times larger part of the field of view. This is particularly relevant for faint transients in the the Galactic Bulge.

## 6. Spectral simulations

While IROS is most effective in image processing and will provide a complete list of point sources detected in the field of view with flux inferences at an accuracy of up to typically a few percent (e.g., Goldwurm & Gros 2022), MLM, although also capable of producing images but at high CPU cost (see Appendix A), excels in the detailed analysis of those sources, in particular the determination of the high-resolution time history of their flux and their spectrum. We here show the spectral capability of MLM. One of the sources in Galactic Center field, GRO J1655-40, is simulated with the following spectral ingredients that are inspired by the spectra of black hole X-ray binaries in their hard state (e.g., review by Kalemcı et al. 2022):

- A continuum consisting of a power law with a photon index of 1.86 and a normalization of  $1.14 \text{ phot s}^{-1} \text{ cm}^{-2} \text{ keV}^{-1}$  at 1 keV. This implies a brightness of 200 mCrab for this source, ignoring the line contributions below which are substantially smaller.
- Interstellar absorption with  $N_{\text{H}} = 0.61 \cdot 10^{22} \text{ cm}^{-2}$ , through the photoionization cross sections of Verner & Yakovlev (1995) and Verner et al. (1996) and the abundances of Anders & Grevesse (1989)
- A narrow Gaussian emission line at 6.4 keV with an intensity of  $0.00263 \text{ phot s}^{-1} \text{ cm}^{-2}$ . This line has an equivalent width of 60 eV.
- A Laor emission line profile at 6.91 keV from an accretion disk surface with an emissivity dependence that is proportional to  $R^{-3}$ , an inner radius of  $1.235 \text{ GM}/c^2$ , an outer radius of  $400 \text{ GM}/c^2$ , an inclination of the disk to the line of sight of 30 degrees and an intensity of  $0.0189 \text{ phot s}^{-1} \text{ cm}^{-2}$ . This line has an equivalent width of 600 eV.

We applied MLM to reconstruct the spectrum for GRO J1655-40 and model it with the 4 components above, using XSPEC version 12.15.1 (Arnaud 1996) with the public response functions for the WFM. The result is shown in Fig. 12. We were able to reproduce the free model parameters as follows:  $N_{\text{H}} = (1.63 \pm 0.44) \cdot 10^{22} \text{ cm}^{-2} = +2.3\sigma$ ,  $\Gamma = 1.90 \pm 0.03 = +1.2\sigma$ , PL-normalization= $1.268 \pm 0.104 \text{ phot s}^{-1} \text{ cm}^{-2} \text{ keV}^{-1} = +1.2\sigma$ , narrow Gauss line  $E = 6.40 \pm 0.08 \text{ keV} = 0.0\sigma$ , narrow Gauss line intensity is  $0.0026 \pm 0.0008 = -0.1\sigma$ , Laor line  $E = 6.90 \pm 0.06 \text{ keV} = -0.1\sigma$ , Laor line intensity is  $0.0238 \pm 0.003 \text{ phot s}^{-1} \text{ cm}^{-2} = +1.6\sigma$ . Therefore, MLM reproduces the multi-component spectrum of this 200 mCrab source accurately.

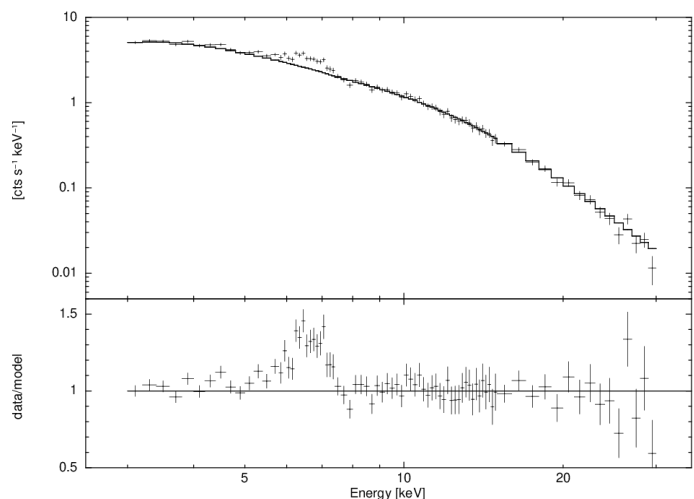


**Fig. 12.** Top panel: MLM reconstruction of the spectrum of GRO J1655-40 (data points) and best-fit model spectrum (drawn histogram). For details, see main text. Bottom panel: comparison between data points and model, after setting the normalizations of the two spectral lines to zero.

## 7. Conclusion and future work

We have developed and verified the performance of three independent software packages for application in the WFM: WISEMAN, to simulate the instrument complete signal chain from celestial X-ray sources to event data streams; IROS, to reconstruct iteratively and fast the sky image from the coded detector data for a particular observation; MLM, to quickly determine the fluxes for all X-ray sources in the field of view for any time interval within the observation and any photon energy interval. We find consistent results throughout which support the validation of all three software packages.

Experimentation with the software has shown that the concept of a pair of identical orthogonal 1.5D coded aperture cameras performs equally well as one 2D coded cameras of the same fine angular resolution, with the same field of view and an equal detector area as both 1.5D cameras combined, except for faint transients in the Galactic Bulge. The advantages of this  $2 \times 1.5D$  setup are that it is possible to use light-weight low-power consumption SDDs and that some level of redundancy is built in. The disadvantage is that the larger cross-like PSF introduces an increased level of source confusion and cross talk between sources when they are on each other's PSF, but at the brightness range that such a camera would be active the source confusion is not an important issue except perhaps in the Galactic Center region.

Our work confirms end-to-end the feasibility of the WFM concept. Its modularity makes it easily adaptable to any mission/observatory concept and low-risk due to the implicit redundancy.

The simulation software enables to test different configurations of the WFM and mask pattern, and the vulnerability to imperfections such as slight misalignments between SDDs in one camera, between mask and detector plane and between cameras in a pair. Regarding the latter, the independent functionality of a single camera comes in handy. Future work will focus on the verification of the alignment budget, experimentation with the mask pattern resolution to align with improvements in SDD spatial resolution, with timing resolution and with spectral resolution in the signal chain.

*Acknowledgements.* This work was performed by the eXTP-WFM Simulations Working Group that was active in 2020-2024 until the WFM instrument was removed from eXTP. Support was provided by INAF Rome, SRON and ICE-CSIC Barcelona. The employed software builds on earlier software written for missions BeppoSAX, AGILE, CGRO and INTEGRAL. We acknowledge all colleagues that were involved in writing the code. It is noted that no AI tool has been employed in the coding, data analysis or manuscript preparation.

## References

- Abdo, A. A., Ackermann, M., Ajello, M., et al. 2009, *ApJS*, 183, 46
- Ables, J. G. 1968, *PASA*, 1, 172
- Anders, E. & Grevesse, N. 1989, *Geochim. Cosmochim. Acta*, 53, 197
- Arnaud, K. A. 1996, in *Astronomical Society of the Pacific Conference Series*, Vol. 101, *Astronomical Data Analysis Software and Systems V*, ed. G. H. Jacoby & J. Barnes, 17
- Barthelmy, S. D., Barbier, L. M., Cummings, J. R., et al. 2005, *Space Sci. Rev.*, 120, 143
- Baumert, L. D. 1971, *Cyclic Difference Sets*
- Braga, J. 2020, *PASP*, 132, 012001
- Brandt, S., Hernanz, M., Alvarez, L., et al. 2014, in *Society of Photo-Optical Instrumentation Engineers (SPIE) Conference Series*, Vol. 9144, *Space Telescopes and Instrumentation 2014: Ultraviolet to Gamma Ray*, ed. T. Takahashi, J.-W. A. den Herder, & M. Bautz, 91442V
- Brown, C. 1974, *Journal of Applied Physics*, 45, 1806
- Campana, R., Feroci, M., Del Monte, E., et al. 2012, in *Society of Photo-Optical Instrumentation Engineers (SPIE) Conference Series*, Vol. 8443, *Space Telescopes and Instrumentation 2012: Ultraviolet to Gamma Ray*, ed. T. Takahashi, S. S. Murray, & J.-W. A. den Herder, 84435O
- Campana, R., Zampa, G., Feroci, M., et al. 2011, *Nuclear Instruments and Methods in Physics Research A*, 633, 22
- Caroli, E., Stephen, J. B., Di Cocco, G., Natalucci, L., & Spizzichino, A. 1987, *Space Sci. Rev.*, 45, 349
- Cash, W. 1979, *ApJ*, 228, 939
- Ceraudo, F., Evangelista, Y., Hernanz, M., et al. 2024, in *Society of Photo-Optical Instrumentation Engineers (SPIE) Conference Series*, Vol. 13093, *Space Telescopes and Instrumentation 2024: Ultraviolet to Gamma Ray*, ed. J.-W. A. den Herder, S. Nikzad, & K. Nakazawa, 130936T
- de Boer, H., Bennett, K., Bloemen, H., et al. 1992, in *Data Analysis in Astronomy*, ed. V. di Gesu, L. Scarsi, R. Buccheri, & P. Crane, 241–249
- Del Monte, E., Ceraudo, F., Della Casa, G., et al. 2024, in *Society of Photo-Optical Instrumentation Engineers (SPIE) Conference Series*, Vol. 13093, *Space Telescopes and Instrumentation 2024: Ultraviolet to Gamma Ray*, ed. J.-W. A. den Herder, S. Nikzad, & K. Nakazawa, 130931U
- Dicke, R. H. 1968, *ApJ*, 153, L101
- Donnarumma, I., Evangelista, Y., Campana, R., et al. 2012, in *Society of Photo-Optical Instrumentation Engineers (SPIE) Conference Series*, Vol. 8443, *Space Telescopes and Instrumentation 2012: Ultraviolet to Gamma Ray*, ed. T. Takahashi, S. S. Murray, & J.-W. A. den Herder, 84435Q
- Eadie, W. T., Drijard, D., & James, F. E. 1971, *Statistical methods in experimental physics*, 231
- Evangelista, Y. 2010, PhD thesis, Università Degli Studi Di Roma 'La Sapienza'
- Falcone, A. D., Colosimo, J. M., Wages, M., et al. 2024, in *Society of Photo-Optical Instrumentation Engineers (SPIE) Conference Series*, Vol. 13093, *Space Telescopes and Instrumentation 2024: Ultraviolet to Gamma Ray*, ed. J.-W. A. den Herder, S. Nikzad, & K. Nakazawa, 1309317
- Fenimore, E. E. & Cannon, T. M. 1978, *Appl. Opt.*, 17, 337
- Fenimore, E. E. & Cannon, T. M. 1981, *Appl. Opt.*, 20, 1858
- Feroci, M., Costa, E., Del Monte, E., et al. 2010, *A&A*, 510, A9
- Feroci, M., Stella, L., van der Klis, M., et al. 2012, *Experimental Astronomy*, 34, 415
- Givaudan, A., Bégoc, S., Bertoli, W., et al. 2024, in *Society of Photo-Optical Instrumentation Engineers (SPIE) Conference Series*, Vol. 13093, *Space Telescopes and Instrumentation 2024: Ultraviolet to Gamma Ray*, ed. J.-W. A. den Herder, S. Nikzad, & K. Nakazawa, 1309370
- Godet, O., Nasser, G., Atteia, J., et al. 2014, in *Society of Photo-Optical Instrumentation Engineers (SPIE) Conference Series*, Vol. 9144, *Space Telescopes and Instrumentation 2014: Ultraviolet to Gamma Ray*, ed. T. Takahashi, J.-W. A. den Herder, & M. Bautz, 91442A
- Goldwurm, A. & Gros, A. 2022, in *Handbook of X-ray and Gamma-ray Astrophysics*, ed. C. Bambi & A. Sanganello, 15
- Gottesman, S. R. & Fenimore, E. E. 1989, *Appl. Opt.*, 28, 4344
- Hammersley, A. 1986, PhD thesis, University of Birmingham
- Hammersley, A., Ponman, T., & Skinner, G. 1992, *Nuclear Instruments and Methods in Physics Research A*, 311, 585
- Hernanz, M., Brandt, S., Feroci, M., et al. 2018, in *Society of Photo-Optical Instrumentation Engineers (SPIE) Conference Series*, Vol. 10699, *Space Telescopes and Instrumentation 2018: Ultraviolet to Gamma Ray*, ed. J.-W. A. den Herder, S. Nikzad, & K. Nakazawa, 1069948
- Hernanz, M., Brandt, S., in't Zand, J., et al. 2022, in *Society of Photo-Optical Instrumentation Engineers (SPIE) Conference Series*, Vol. 12181, *Space Telescopes and Instrumentation 2022: Ultraviolet to Gamma Ray*, ed. J.-W. A. den Herder, S. Nikzad, & K. Nakazawa, 121811Y
- Hernanz, M., Feroci, M., Evangelista, Y., et al. 2024, in *Society of Photo-Optical Instrumentation Engineers (SPIE) Conference Series*, Vol. 13093, *Space Telescopes and Instrumentation 2024: Ultraviolet to Gamma Ray*, ed. J.-W. A. den Herder, S. Nikzad, & K. Nakazawa, 130931Y
- Högbom, J. A. 1974, *A&AS*, 15, 417
- in 't Zand, J. J. M. 1992, PhD thesis, Netherlands Institute for Space Research
- in 't Zand, J. J. M., Heise, J., & Jager, R. 1994, *A&A*, 288, 665
- in 't Zand, J. J. M., Kuiper, L., Amati, L., et al. 2000, *ApJ*, 545, 266
- Jager, R., Mels, W. A., Brinkman, A. C., et al. 1997, *A&AS*, 125, 557
- Kalemci, E., Kara, E., & Tomsick, J. A. 2022, in *Handbook of X-ray and Gamma-ray Astrophysics*, ed. C. Bambi & A. Sanganello, 9
- Kirsch, M. G., Briel, U. G., Burrows, D., et al. 2005, in *Society of Photo-Optical Instrumentation Engineers (SPIE) Conference Series*, Vol. 5898, *UV, X-Ray, and Gamma-Ray Space Instrumentation for Astronomy XIV*, ed. O. H. W. Siegmund, 22–33
- Klebesadel, R. W., Strong, I. B., & Olson, R. A. 1973, *ApJ*, 182, L85
- Levine, A. M., Bradt, H., Cui, W., et al. 1996, *ApJ*, 469, L33
- Levine, A. M., Bradt, H., Morgan, E. H., Remillard, R., & MIT/GSFC ASM Team. 2006, *Advances in Space Research*, 38, 2970
- Levine, A. M., Bradt, H. V., Chakrabarty, D., Corbet, R. H. D., & Harris, R. J. 2011, *ApJS*, 196, 6
- Marshall, F. E., Boldt, E. A., Holt, S. S., et al. 1980, *ApJ*, 235, 4
- Matsuoka, M., Kawasaki, K., Ueno, S., et al. 2009, *PASJ*, 61, 999
- Mattox, J. R., Bertsch, D. L., Chiang, J., et al. 1996, *ApJ*, 461, 396
- Meißner, T., Rozhkov, V., Hesser, J., Nahm, W., & Loew, N. 2023, *Journal of Instrumentation*, 18, P01006
- Nottingham, M. R. 1993, PhD thesis, University of Birmingham
- Palmieri, T. M. 1974, *Ap&SS*, 28, 277
- Pollock, A. M. T., Bignami, G. F., Hermsen, W., et al. 1981, *A&A*, 94, 116
- Ray, P. S., Roming, P. W. A., Argan, A., et al. 2024, *Journal of Astronomical Telescopes, Instruments, and Systems*, 10, 042504
- Remillard, R. A., Hernanz, M., Zand, J. i., et al. 2024, *Journal of Astronomical Telescopes, Instruments, and Systems*, 10, 042505
- Rideout, R. M. 1995, PhD thesis, University of Birmingham
- Rideout, R. M. & Skinner, G. K. 1996, *A&AS*, 120, 579
- Sims, M., Turner, M. J. L., & Willingale, R. 1980, *Space Science Instrumentation*, 5, 109
- Skinner, G. K. 2008, *Appl. Opt.*, 47, 2739
- Skinner, G. K. & Nottingham, M. R. 1993, *Nuclear Instruments and Methods in Physics Research A*, 333, 540
- Tamagawa, T., Enoto, T., Kitaguchi, T., et al. 2025, *PASJ*, 77, 466
- Valinia, A. & Marshall, F. E. 1998, *ApJ*, 505, 134
- Verner, D. A., Ferland, G. J., Korista, K. T., & Yakovlev, D. G. 1996, *ApJ*, 465, 487
- Verner, D. A. & Yakovlev, D. G. 1995, *A&AS*, 109, 125
- Verrecchia, F., in't Zand, J. J. M., Giommi, P., et al. 2007, *A&A*, 472, 705
- Wilks, S. S. 1938, *Annals of Mathematical Statistics*, 9, 60
- Willingale, R. 1981, *MNRAS*, 194, 359
- Yuan, W., Zhang, C., Chen, Y., & Ling, Z. 2022, in *Handbook of X-ray and Gamma-ray Astrophysics*, ed. C. Bambi & A. Sanganello, 86
- Zhang, C., Ling, Z. X., Sun, X. J., et al. 2022, *ApJ*, 941, L2
- Zhang, S., Santangelo, A., Feroci, M., et al. 2019, *Science China Physics, Mechanics, and Astronomy*, 62, 29502
- Zwart, F., Tacken, R., in't Zand, J. J. M., et al. 2022, in *Society of Photo-Optical Instrumentation Engineers (SPIE) Conference Series*, Vol. 12181, *Space Telescopes and Instrumentation 2022: Ultraviolet to Gamma Ray*, ed. J.-W. A. den Herder, S. Nikzad, & K. Nakazawa, 1218167

## Appendix A: MLM on GC field

MLM can be employed to generate images. An example is shown in Fig. A.1, for part of the GC sky image. For this exercise, GX 5-1 was included in  $\mathcal{H}_0$  and the image was generated by scanning the field of view for deviations from  $\mathcal{H}_0$ . As said, this is a computationally intensive exercise. The generation of this image, which covers only 8% of the field of view, took approximately 24 hr on a Linux Debian system with a 12th generation Intel(R) Core(TM) i7-12700K CPU.

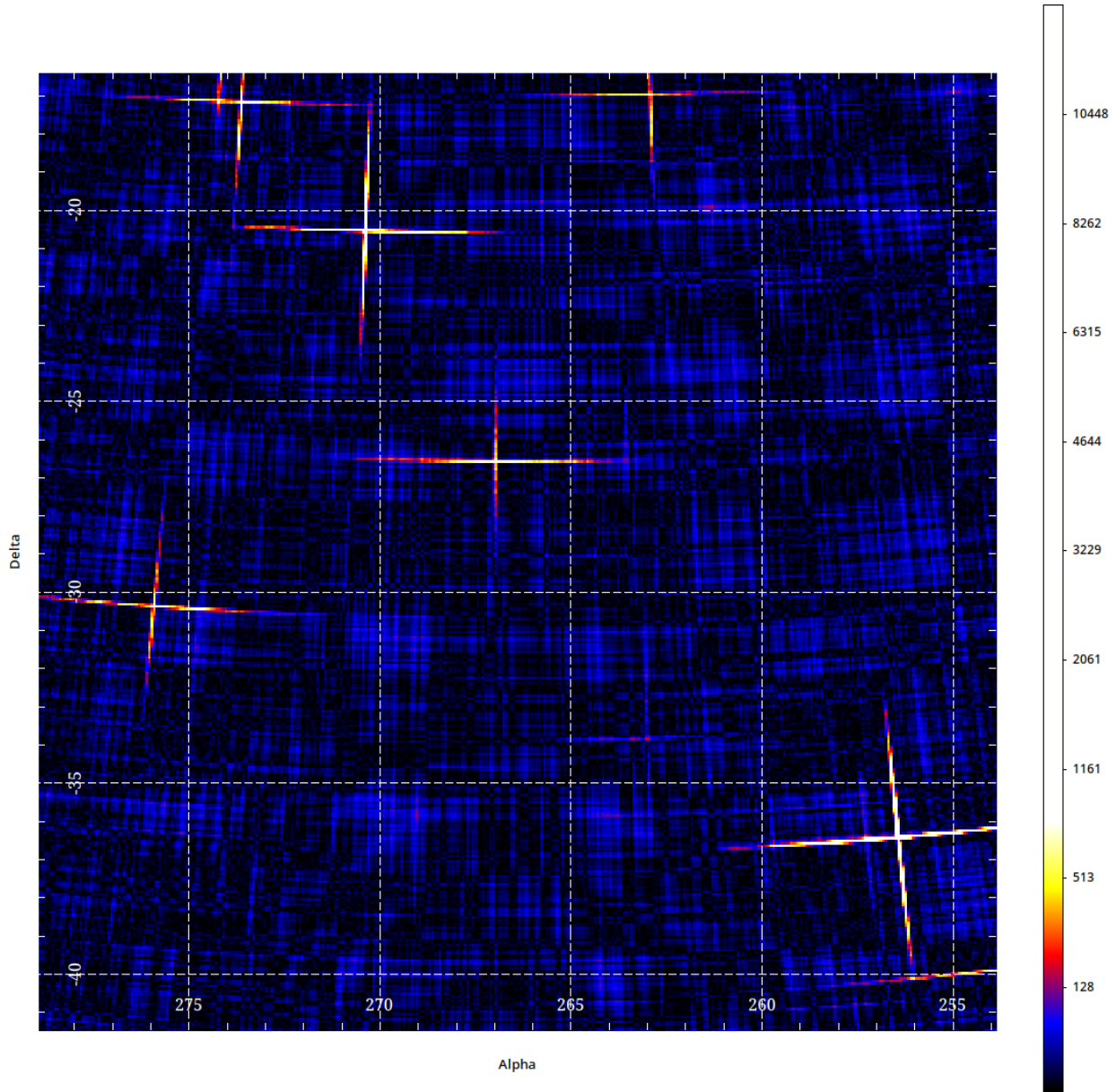


**Fig. A.1.** MLM solution of the central  $25 \times 25$  square degrees of the GC observation, projected on an R.A.-Decl. plane (Eq. 2000.0). Sources are 4U 1820-30 at (R.A., Decl.)=(275.9,-30.4), GX 9+1 at (270.4,-20.5), GX 3+1 at (267.0,-26.5), GX 9+9 at (262.2,-17.0), GX 13+1 at (273.6,-17.2), GX 354-0 at (263.0,-33.8), GX 349+2 at (256.4,-36.4) and partially GRO J1655-40 at (353.5,-39.8). GX 5-1 is missing at (270.3,-25.1) because it is included in  $\mathcal{H}_0$ . The pixel scale is  $Q$  (proxy for significance).

## Appendix B: Complete eXTP-WFM simulation

In order to show what the potential is of a complete WFM instrument, we have simulated an observation centered close to the Galactic Center (i.e., GX 3+1) for the Sun position on March 15 for 3 camera pairs as would have been applicable for eXTP. The IROS solution is shown in Fig. B.1. This single observation covers the Galactic plane between  $-100$  and  $+100$  degrees in Galactic longitude and a substantial range of latitudes above and below the plane. It covers 40% of the sky (5.0 sr). It also covers 75% of all ASM sources and bright Galactic X-ray sources and 83% of all bright ASM sources (i.e., with an average flux higher than 10 mCrab). There are a few sources which are in overlapping FOVs of 2 adjacent camera pairs. These show double crosses at a small angle. Thus, the source confusion increases somewhat in these overlap regions but is partly compensated by an increased sensitivity.

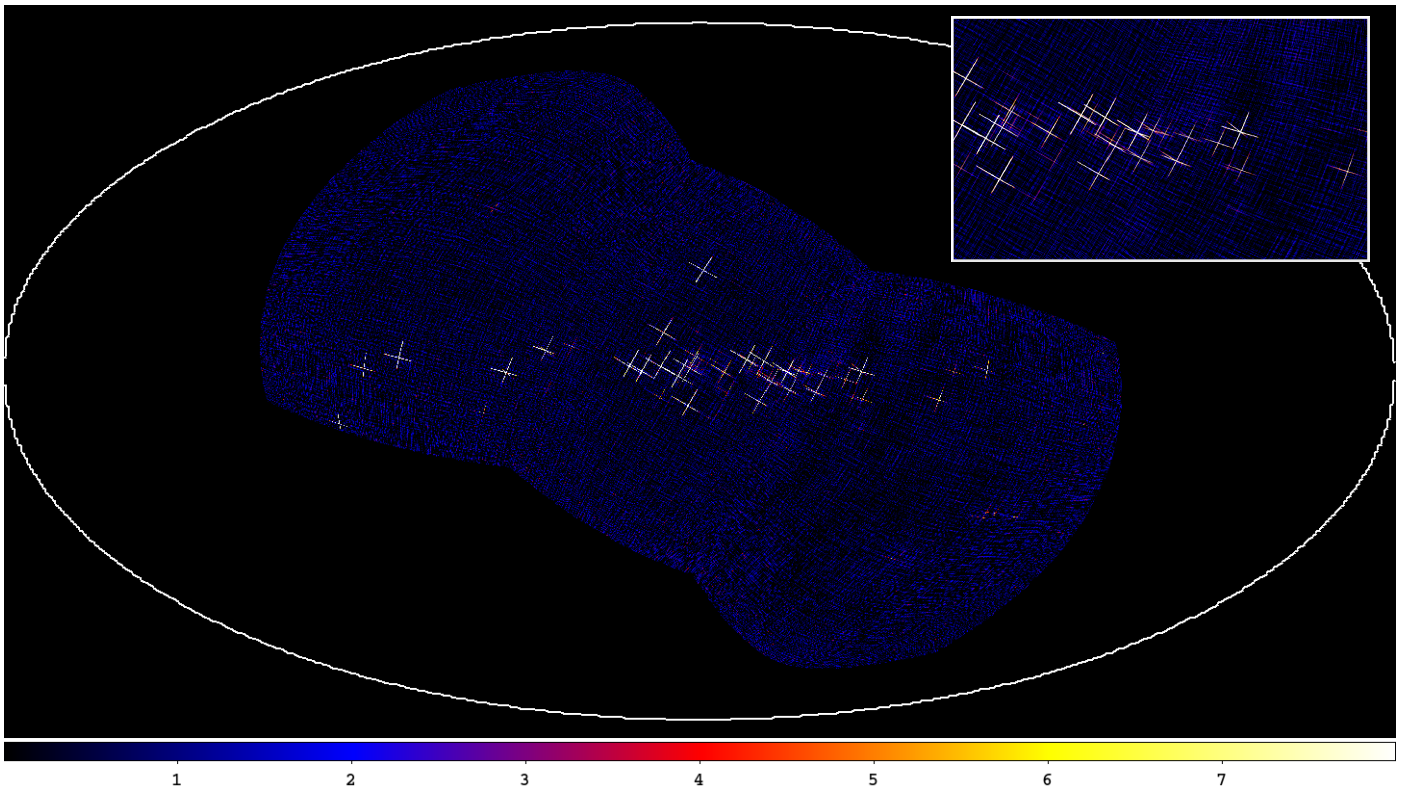


**Fig. B.1.** Example of an IROS solution of a 10 ksec eXTP-WFM (N=3) observation of GX 3+1 for the Sun position on March 15, mapped in an Aitoff projection in Galactic coordinates. The color scale is mapped between 0 and 8 significance. The inset shows a zoomed-in region where the field of views of two camera pairs overlap.